Volume 1 | Number 1 | Jan 2013 | Pages 1–100

Journal of
Materials Chemistry A

Materials for energy and sustainability
www.rsc.org/materialsA

ROYAL SOCIETY
OF CHEMISTRY

ROYAL SOCIETY
OF CHEMISTRY

www.rsc.org/materialsA

ARTICLE TYPE

A graphene/carbon nanotube@π-conjugated polymer nanocomposite for high-performance organic supercapacitor electrode

Minqiang Sun,[a] Gengchao Wang,*[a] Chongyang Yang,[a] Hao Jiang[a] and Chunzhong Li[a]

The supercapacitors based on π-conjugated conducting polymers have attracted significant attention due to high pseudocapacitance. However, the narrow potential window (<1 V) gives rise to low energy density, which restricts practical applications. Here, a novel hierarchical graphene nanosheets/acid-treated multi-walled carbon nanotube-supported poly(1,5-diaminoanthraquinone) (GNS/*a*MWCNT@PDAA)
10 nanocomposite is successfully synthesized using optimal $Ce(SO_4)_2$ oxidant and camphorsulfonic acid dopant. The as-prepared nanocomposite displays unique nanoporous morphology, high π-conjugated degree and excellent conductive interpenetrating network. With the intriguing features as well as unique p- and n-doping characteristic, the as-fabricated supercapacitor in 1 M Et_4NBF_4-AN electrolyte can be reversibly cycled in the potential window of 2.8 V and achieves superhigh energy density of 86.4 Wh kg^{-1}
15 at power density of 0.73 kW kg^{-1}, which still retains 55.5 Wh kg^{-1} even at power density of 153.9 kW kg^{-1}. Furthermore, superior cycling stability is achieved with only 7 % capacitance loss after 10000 cycles. The state-of-the-art performance has surpassed that of most recently reported supercapacitors, thus representing a significant breakthrough in the π-conjugated polymers-based supercapacitors.

1. Introduction

20 Parallel to the fast-growing demand for portable electronics and electric vehicles, developing efficient and renewable energy storage systems has become a global concern.[1-6] Supercapacitors, with desirable characteristics of high power density, fast charging (with seconds) and long cycle life, have been widely recognized
25 as an important class of energy storage devices.[7,8] Nowadays, the supercapacitor technology is dedicated to pursuing high energy density without sacrificing power density and cycle life.[9,10] According to the equation $E = 0.5CV^2$, the energy density can be improved by maximizing the specific capacitance (C) and/or the
30 potential window (V).[11] Although carbonaceous materials possess broad potential window, the specific capacitance is relatively low, which brings about the unsatisfactory energy density. Conducting polymers (CPs), such as polyaniline and polypyrrole with p-doping characteristic, only exhibit high
35 pseudocapacitance in narrow potential window.[12-15] In this regard, an efficient approach is to develop asymmetric supercapacitors for widening potential window.[16,17] Alternatively, it is more advisable to explore new-generation CPs with both p- and n-doping capability, which can achieve excellent
40 pseudocapacitance in broad potential window and perfectly accord with the demand for energy density.

Recently, a novel π-conjugated polymer called poly(1,5-diaminoanthraquinone) (PDAA), whose raw materials are abundant and can be synthesized from the biomass, has roused
45 research interests.[18-20] Through hybridizing polyaniline backbones (p-doping) with electroactive 1,4-benzoquinone

moiety of high capacity (n-doping), PDAA possesses excellent pseudocapacitance characteristics in broad potential window than the polyaniline alone.[21-23] Moreover, strong π-π stacking
50 interaction among anthracene rings and hydrogen bonds between N-H and C=O groups make PDAA inclined to form "supramolecular" structure, leading to superior cycling stability compared to other reported CPs.[24-27] Unfortunately, the previously reported PDAAs exhibit lower conductivity[23,24] and
55 densely packed structure of the PDAA by conventional polymerization methods makes the expected outstanding performance significantly vanish.

To overcome these drawbacks, a homogeneous nano-sized and well-ordered structure must be considered for the advancement of
60 inherent performance.[28-32] Moreover, the incorporation of carbonaceous materials into nanostructured CPs has attracted great interest owing to the enhanced properties arising from high conductivity and reinforcement of carbon nanofillers.[33-36] To date, numerous nanocomposites of graphene/CPs,[13,36-40] carbon
65 nanotube/CPs,[34,41-45] mesoporous carbon/CPs[35,46,47] and graphene/carbon nanotube/CPs[48-51] have been explored, among which, graphene/carbon nanotube/CPs remarkably increase the accessible surface for CPs deposition. In particular, the materials with high porosity are of great significance for energy storage,
70 which largely allows electrolytes to freely diffuse inside the internal space.[52-54]

Herein, we ingeniously develop a novel hierarchical porous nanocomposite based on graphene nanosheets/acid-treated multi-walled carbon nanotube-supported poly(1,5-
75 diaminoanthraquinone) (GNS/*a*MWCNT@PDAA). To make full

play of intrinsic performance of GNS, the GNS/aMWCNT is mildly reduced by ^{60}Co γ-ray irradiation to effectively restrain the aggregation, on which the nanostructured PDAA is firmly deposited via π-π stacking interaction. In addition, the camphorsulfonic acid (CSA), not only a dopant for PDAA but also a soft template for the polymerization, is adopt, which perfectly achieves the nanoporous structure for the nanocomposite. The formation process in detail is displayed in Scheme 1. Furthermore, due to unique p- and n-doping capability, GNS/aMWCNT@PDAA is wisely constructed as both positive

and negative electrodes for organic supercapacitors, bringing about a significant improvement of energy density and cycling performance. The as-fabricated supercapacitor in 1 M Et$_4$NBF$_4$-AN electrolyte achieves a maximum energy density of 86.4 Wh kg^{-1} at a power density of 0.73 kW kg^{-1} as well as superior cycling stability with only 7 % capacitance loss after 10000 cycles. These encouraging results represent a significant breakthrough in the development of π-conjugated CPs for promising organic supercapacitors.
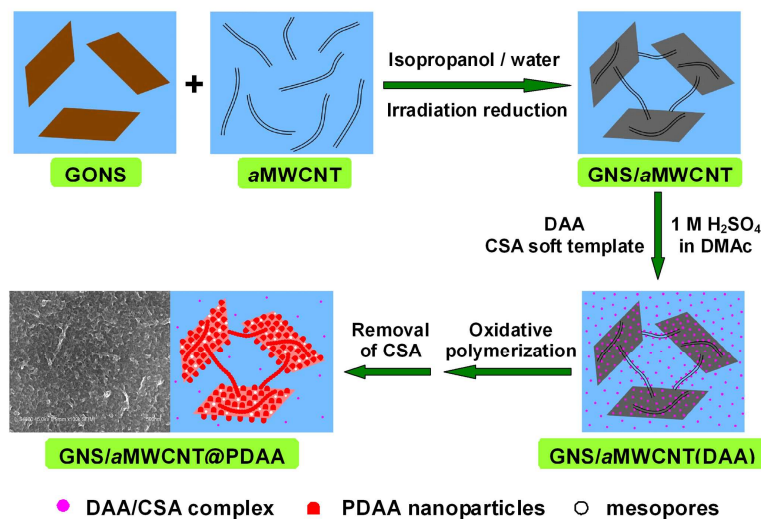
Scheme 1 Schematic illustration for the formation process of hierarchical porous GNS/aMWCNT@PDAA nanocomposite.

2. Experimental

2.1 Preparation of GNS/aMWCNT

Graphite oxide was synthesized from natural graphite powder (Shanghai Yifan Graphite Co. Ltd.) by a modified Hummers method.[55] As-prepared graphite oxide was exfoliated in pH =10 ammonia solution under ultrasonication for 40 min. The resulting graphene oxide nanosheets (GONS) were centrifuged at 3000 rpm to remove the aggregations. The aMWCNT was prepared via mixed acid treatment of MWCNT (diameter < 8 nm, Chengdu Organic Chemicals Co. Ltd.).[56]

The GONS and aMWCNT aqueous dispersions were mixed under stirring to form three-dimensional interpenetrating GONS/aMWCNT (the weight ratio of GONS to aMWCNT was 70/30). Subsequently, the GNS/aMWCNT was prepared by irradiation reduction technique. The isopropanol was added into the above GONS/aMWCNT to obtain isopropanol/water dispersion (50/50, v/v) with a final concentration of 1 mg mL^{-1}, which was then deoxygenated by argon bubbling for 30 min and sealed in stainless steel pipe with argon atmosphere. Finally, the stainless steel pipe was irradiated through ^{60}Co γ-ray with the irradiation dose of 100 kGy to obtain the GNS/aMWCNT.

2.2 Synthesis of GNS/aMWCNT@PDAA nanocomposite

The GNS/aMWCNT was prepared by ^{60}Co γ-ray irradiation reduction technique and the detailed process was shown in Electronic Supporting Information. The GNS/aMWCNT@PDAA nanocomposite was synthesized by a chemically oxidative

polymerization method. Typical procedure was as follows: 25 mg GNS/aMWCNT was added into 15 mL 1 M H$_2$SO$_4$ DMAc solution under ultrasonication for 1 h to obtain well-dispersed suspension followed by the addition of camphorsulfonic acid (CSA, 0.63 mmol). After that, 0.63 mmol DAA monomer (7.5 mL 1 M H$_2$SO$_4$ DMAc solution) was added into the above suspension, which was continuously stirred for 4 h. Then, half oxidant of Ce(SO$_4$)$_2$ (0.63 mmol, 7.5 mL 1 M H$_2$SO$_4$ DMAc solution) was added by dropwise and another half added after 2 h. The reaction was carried out at 20 °C for 48 h with final DAA mole concentration of 0.017 mol L^{-1}. Finally, the resulting product was washed with DMAc, ethanol and distilled water for several times and afterwards freeze dried for use. For comparison, pure PDAA doped with CSA and without CSA was synthesized through the similar procedure above without the presence of GNS/aMWCNT.

2.3 Synthesis of GNS/aMWCNT@polyaniline (PANI) nanocomposite

The GNS/aMWCNT@PANI nanocomposite was synthesized by a chemically oxidative polymerization method. Typical procedure was as follows: 25 mg GNS/aMWCNT was added into 15 mL 1 M H$_2$SO$_4$ aqueous solution under ultrasonication for 1 h to obtain well-dispersed suspension followed by the addition of camphorsulfonic acid (CSA, 0.63 mmol). After that, 0.63 mmol aniline monomer (7.5 mL 1 M H$_2$SO$_4$ solution) was added into the above suspension, which was continuously stirred for 4 h. Then, half oxidant of ammonium persulfate (APS, 0.63 mmol, 7.5 mL 1 M H$_2$SO$_4$ solution) was added by dropwise and another half

was added after 2 h. The reaction was carried out at 20 °C for 48 h with final aniline mole concentration of 0.017 mol L^{-1}. Finally, the resulting product was washed with ethanol and distilled water for several times and afterwards freeze dried for use.

2.4 Characterization

The Fourier transform infrared spectroscopy (FTIR) spectra were recorded at a Nicolet 5700 spectrometer from KBr pellets. Raman spectra were recorded on a Renishaw inVia+Reflex using a 50mW He-Ne laser operated at 514 nm. X-ray diffraction (XRD) data were collected from 5° to 50° (2θ-angle) from a Rigaku D/Max 2550 VB/PC X-ray diffractometer using Cu K_α radiation. The morphologies of the samples were characterized by the field-emission scanning electron microscopy (FE-SEM, Hitachi S-4800) with an energy dispersive spectrometer (EDS, QUANTAX 400-30) and the transmission electron microscope (TEM, JEOL JEM-1400, 100 kV). Atomic Force Microscopy (AFM) images were obtained with a multimode atomic force microscopy (NanoscopeIIIa, Veeco), employing the uncontact mode. X-ray photoelectron spectroscopy (XPS) analysis was performed in a thermo scientific ESCALAB 250Xi X-ray photoelectron spectrometer equipped with amonochromatic Al Kα X-ray source (1486.6 eV). Nitrogen adsorption-desorption isotherms were performed using a Micromeritics ASAP 2020 analyzer at 77 K. Before measurements, the samples were degassed in vacuum at 353 K for 4 h. The specific surface area and the pore size distribution were calculated using the BET and slit/cylindrical nonlocal DFT (NLDFT) methods, respectively. The conductivity of the samples was determined by SX 1934 four-probe instrument using compressed pellets.

2.5 Electrochemical measurements

The working electrodes were prepared by mixing 70 wt% active materials, 20 wt% acetylene black and 10 wt% binder (LA132, dissolved in deionized water/ethanol mixed solution) to form a slurry, which was uniformly coated on Toray carbon paper (TCP) with diameter of 12 mm. The resulting electrode was then dried in vacuum oven (80 °C) overnight to remove ethanol and moisture. The mass loading of active materials on TCP was carefully controlled to be *ca.* 1 mg.

Both three- and two-electrode cell configurations were used to measure the electrochemical performance of active materials as supercapacitor electrodes in organic electrolyte (1 M Et_4NBF_4-AN). In three-electrode system, Pt slice and Ag/Ag^+ electrode were used as the counter electrode and reference electrode, respectively. The cyclic voltammetry (CV) and galvanostatic charge/discharge tests were performed with an Autolab electrochemical workstation inside an Ar-filled glove box.

The two-electrode configuration (2016 stainless-steel coin cell) with two symmetrical active materials as both positive and negative electrodes, sandwiched by polypropylene separator (25 μm thick, Celgard 3501), was assembled in glove box. The CV, galvanostatic charge/discharge and electrochemical impedance spectroscopy (EIS) were also carried out by a CHI660D electrochemical workstation and cycling stability was conducted on a LAND CT2001A program testing system. It is worth noting that the specific capacitance, power and energy density were calculated based on total mass of positive and negative materials. And the data analysis for electrochemical measurements was

shown in Electronic Supplementary Information.

3. Results and discussion

The GNS/*a*MWCNT@PDAA preparation procedure employed in our study involves a chemically oxidative polymerization of the PDAA grown on GNS/*a*MWCNT as a carrier in 1 M H_2SO_4 DMAc solution. The process was carried out using appropriate $Ce(SO_4)_2$ oxidant and CSA dopant with DAA mole concentration of 0.017 mol L^{-1}. Here, to restrain the aggregation of GNS, the GNS/*a*MWCNT is mildly reduced by ^{60}Co γ-ray irradiation technique, in which GNS are produced through the ring-opening of epoxide groups in GONS induced by alcohol radicals followed by the elimination of gem-diols to form the C=C bonds.[57] As seen from EDS result (Fig. 1a), the oxygen content (12.4 wt%) of GNS/*a*MWCNT markedly decreases compared to GONS/*a*MWCNT (30.3 wt%), demonstrating that oxygen-containing groups are successfully reduced by γ-ray irradiation. Moreover, Raman spectra display that the D and G bands for GNS/*a*MWCNT at around 1350 and 1600 cm^{-1} obviously become narrow (Fig. S1†), which implies the improvement of ordered graphitic domains after irradiation.
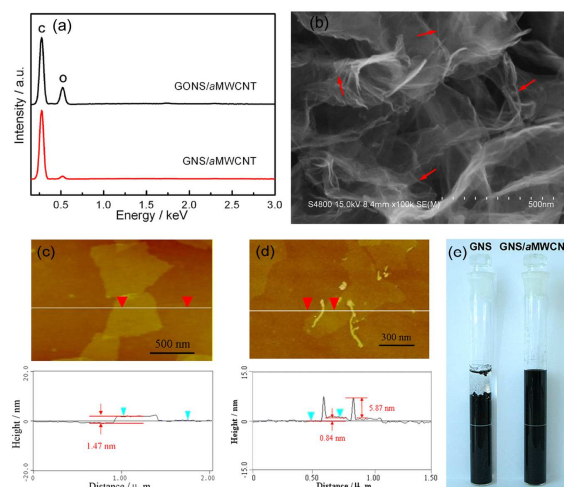

Fig. 1 (a) EDS of GONS/*a*MWCNT and GNS/*a*MWCNT. (b) FE-SEM image of GNS/*a*MWCNT. AFM images of (c) GNS and (d) GNS/*a*MWCNT with height profiles. (e) The photograph showing GNS and GNS/*a*MWCNT dispersions.

It can be observed from the FE-SEM image of GNS/*a*MWCNT (Fig. 1b) that individual *a*MWCNT (marked by red arrow) appear to be intercalated into thin and crumpled GNS, forming 3D interpenetrating network structure with high accessible surface of 411.8 m^2 g^{-1} (Fig. S2†). In addition, it is detected from atomic force microscopy (AFM) that the thickness of GNS becomes thinner from 1.47 to 0.84 nm after the introduction of *a*MWCNT (Fig. 1c-d). The results further indicate the intercalating effect of *a*MWCNT, which effectively enlarge the space between GNS sheets. Thus, the *a*MWCNT act as steric barriers successfully hindering the irreversible aggregation of GNS, which brings about good dispersion stability for GNS/*a*MWCNT (Fig. 1e). Moreover, the conductivity of GNS/*a*MWCNT after irradiation can reach up to 18.4 S cm^{-1}, which is three orders of magnitude higher than that of GONS/*a*MWCNT (7.8×10^{-3} S cm^{-1}) and also can be superior to that of GNS (12.2 S cm^{-1}). In general, as a

carrier with high conductivity and accessible surface, GNS/*a*MWCNT is beneficial to the growth of nanostructured PDAA.

⁵ The morphology of the GNS/*a*MWCNT@PDAA is characterized by the FE-SEM and TEM. As shown in Fig. 2a, the as-prepared GNS/*a*MWCNT@PDAA displays unique coexisting structure of *a*MWCNT glossily coated with PDAA (marked by red arrow) and GNS evenly covered with dense PDAA nanoparticles (10~40 nm diameter) intercalating a large number ¹⁰ of mesopores with *ca.* 3~20 nm size. Moreover, the TEM image of GNS/*a*MWCNT@PDAA further demonstrates the existence of mesopores (marked by red circle, Fig. 2b), where the conductive interpenetrating network of *a*MWCNT is clearly observed, as expected. In contrast, pure PDAA synthesized through similar ¹⁵ procedure displays unsatisfactory aggregated structure composed of 50~100 nm nanoparticles (Fig. S3†). In addition, in order to make clear the role of CSA, the GNS/*a*MWCNT@PDAA without CSA is synthesized as a comparison. And almost no obvious mesopores are observed from the FE-SEM image (Fig. S4†). ²⁰ Thus, CSA not only serves as a dopant for PDAA but also acts as a soft template to form nanopores during polymerization process.
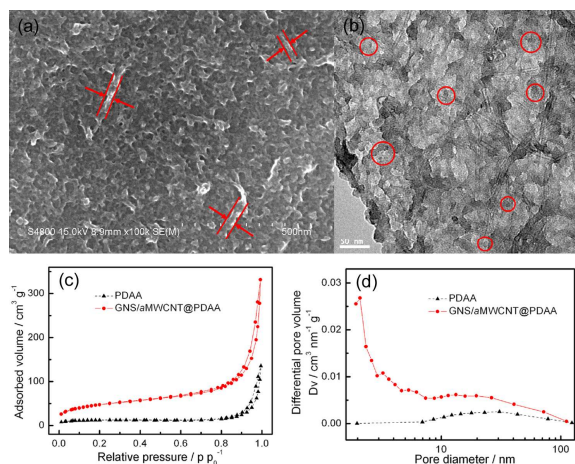

Fig. 2 (a) FE-SEM image and (b) TEM image of GNS/*a*MWCNT@PDAA. (c) N_2 adsorption/desorption isotherms and (d) ²⁵ corresponding pore-size distributions of PDAA and GNS/*a*MWCNT@PDAA.

The N_2 adsorption/desorption isotherms were performed to further investigate the textural characteristics and exposed surface area. As shown in Fig. 2c, the distinct hysteresis loops in the ³⁰ range of 0.8~1.0 P/P_0 suggest the presence of mesopores for PDAA and GNS/*a*MWCNT@PDAA. Notably, except for some pores with 8~100 nm size similar to PDAA, the pore size distribution of GNS/*a*MWCNT@PDAA shows some weak peaks ranging from 3~8 nm and one sharp peak around 2 nm ³⁵ corresponding to the micropores of GNS/*a*MWCNT (Fig. 2d and Fig. S2†). This result indicates a hierarchical porous structure of micro- and mesopores for GNS/*a*MWCNT@PDAA, which is in good accordance with above morphology observation. As a result, the BET surface area of GNS/*a*MWCNT@PDAA is 169.2 ⁴⁰ $m^2\ g^{-1}$ with a total pore volume of 0.49 $cm^3\ g^{-1}$, much higher than that of PDAA (41.9 $m^2\ g^{-1}$, 0.2 $cm^3\ g^{-1}$). From the above, such intriguing morphology and high surface area of GNS/*a*MWCNT@PDAA can substantially improve PDAA utilization and be extremely beneficial to rapid electron transport

⁴⁵ and ion diffusion, thus resulting in enhanced electrochemical performance.

To shed light on the effect of GNS/*a*MWCNT on the chemical structure of PDAA, FTIR spectra were employed. The FTIR spectrum of GNS/*a*MWCNT@PDAA exhibits the main bands at ⁵⁰ 1579, 1488 and 1253 cm^{-1} similar to pure PDAA, corresponding to C=C stretching vibrations of quinoid and benzenoid rings as well as C–N stretching vibration, respectively (Fig. 3a). It is notably found that the intensity of quinoid rings in GNS/*a*MWCNT@PDAA obviously strengthens compared to ⁵⁵ pure PDAA. This fact may suggest that the π-bonded surface of GNS and *a*MWCNT interacts strongly with the quinoid rings of PDAA via π-π electron stacking, which promotes and/or stabilizes the quinoid structure.[58,59] In addition, the PDAA doped with CSA possesses more quinoid rings than the PDAA without ⁶⁰ CSA (Fig. S5†). Thus, the strengthening of quinoid rings for GNS/*a*MWCNT@PDAA is mainly ascribed to the introduction of GNS/*a*MWCNT and CSA doping. The XRD patterns show that GNS/*a*MWCNT@PDAA displays a broad diffraction peak at around 2θ=24.5° similar to pure PDAA, indicating the ⁶⁵ substantially amorphous structure (Fig. 3b). The result implies that the introduction of GNS/*a*MWCNT makes no obvious change on the crystal structure of PDAA.
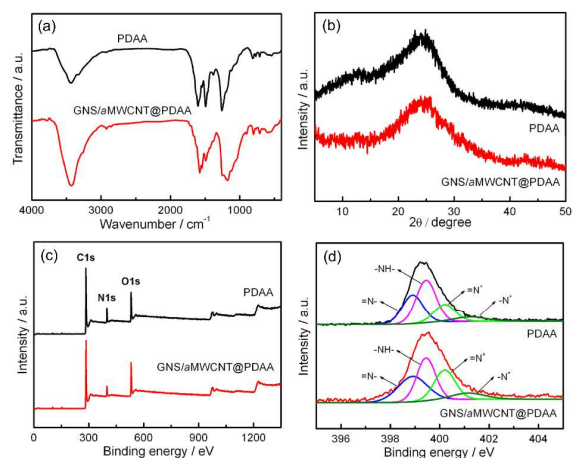

Fig. 3 (a) FTIR spectra, (b) XRD patterns, XPS spectra for (c) survey ⁷⁰ scan and (d) N 1s region of PDAA and GNS/*a*MWCNT@PDAA.

The chemical composition and structure for pure PDAA and GNS/*a*MWCNT@PDAA are further characterized by X-ray photoelectron spectroscopy (XPS). As displayed in Fig. 3c, the GNS/*a*MWCNT@PDAA possesses primary C 1s, N 1s and O 1s ⁷⁵ peaks similar to PDAA and their element contents are listed in Tab. S1†. According to the N content of 8.3 %, the PDAA content in the composite is calculated to be *ca.* 70.6 %. As displayed in Fig. 3d, the signals of N 1s for PDAA and GNS/*a*MWCNT@PDAA can be fitted with peaks of quinonoid ⁸⁰ imine (=N–, 398.9 eV), benzenoid amine (–NH–, 399.5 eV), protonated imine (=N⁺–, 400.2 eV) and protonated amine (–N⁺–, 401.2 eV), respectively, which verifies the formation of π-conjugated polymer like polyaniline. It can be detected from Tab. S1† that $[(=N^+ + -N^+)/N_{total}]$ ratio (0.35) of ⁸⁵ GNS/*a*MWCNT@PDAA is apparently higher than that of PDAA (0.26), implying excellent doping capability for capturing more BF_4^- anions in organic electrolyte. Moreover, higher [=N–/–NH–]

ratio (0.92) is observed from the GNS/*a*MWCNT@PDAA, further indicating richer quinoid rings, which is consistent with above FTIR results.
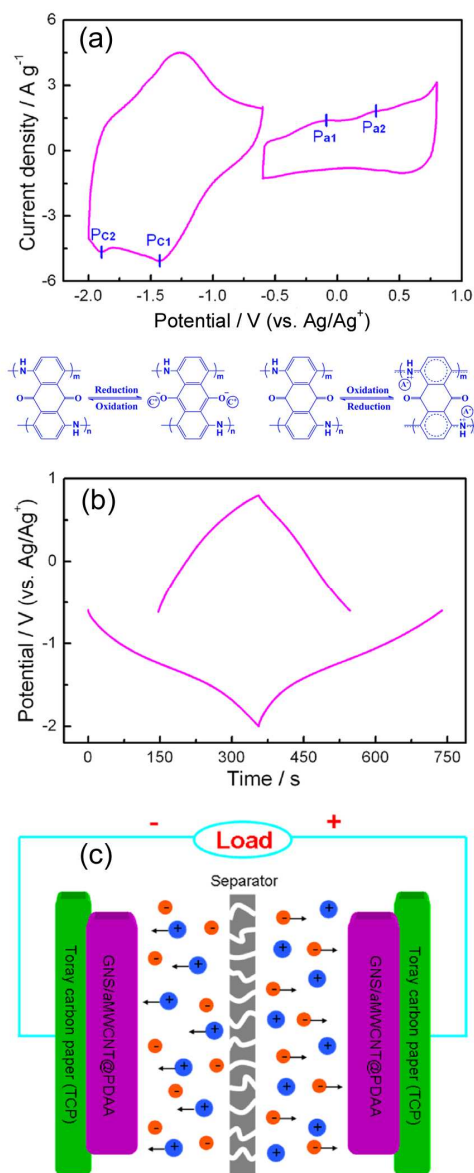

Fig. 4 (a) Comparative CV curves at a scan rate of 10 mV s^{-1} attaching corresponding redox reactions below and (b) comparative charge/discharge curves at a current density of 1 A g^{-1} for GNS/*a*MWCNT@PDAA recorded by a three-electrode system in half potential window for the negative and positive part in 1 M Et$_4$NBF$_4$-AN electrolyte. (c) Charge/discharge schematic illustration of the supercapacitor based on GNS/*a*MWCNT@PDAA as both positive and negative electrodes.

Due to excellent chemical structure and unique morphology, GNS/*a*MWCNT@PDAA can be commendably applied in electrochemical energy storage. Fig. 4a shows cyclic voltammetry (CV) curves for GNS/*a*MWCNT@PDAA measured by three-electrode configuration in 1 M Et$_4$NBF$_4$-AN electrolyte. In relatively negative potential range, a reduction peak (P$_{c1}$) and the corresponding oxidation peak appear at *ca*. -1.43 and -1.27 V, involving a quinine/quinine radical anion (Q/Q$^{\bullet-}$) transition. As the potential is scanned more negative, another reduction peak

(P$_{c2}$) occurred at *ca*. -1.9 V, corresponding to quinine radical anion/quinine dianion (Q$^{\bullet-}$/Q^{2-}) transition. However, no oxidation peak corresponding to the Q^{2-} is observed, suggesting that the Q^{2-} is likely to be chemically modified to produce some form of species (Q$^{\bullet-}$ speculated), which are just oxidized at the same potential of P$_{c1}$. As seen from the corresponding redox reaction below, the Et$_4$N$^+$ cations of the electrolyte compensate for the negative charges of the Q$^{\bullet-}$ and/or Q^{2-} (n-doping). In higher positive potential range, the redox responses basically resemble those for the π-conjugated system of electroactive polyaniline. The polyaniline moiety for PDAA is firstly oxidized to form the radical cations followed by a radical cation/imine cation (=N$^+$−) transition, which correspond to the oxidation peak of P$_{a1}$ (-0.08 V) and P$_{a2}$ (0.31 V), respectively. In this case, the BF$_4^-$ anions are considered to compensate for the positive charges (p-doping).

Furthermore, the charge/discharge curves for GNS/*a*MWCNT@PDAA in half potential window of the negative (-2~-0.6 V) and positive part (-0.6~0.8 V) are shown in Fig. 4b. It is found that the GNS/*a*MWCNT@PDAA exhibits longer discharge duration in relatively negative potential window, which indicates higher specific capacitance, while a short discharge duration in the positive part. Based on the calculation, the specific capacitance can be up to 274 and 137 F g^{-1} in negative and positive potential window, respectively. This indicates that the GNS/*a*MWCNT@PDAA possesses excellent pseudocapacitance characteristics in broader potential window (-2~0.8 V). In comparison, the charge/discharge curves (Fig. S6a†) of GNS/*a*MWCNT@PANI show only a little discharge duration (18.3 F g^{-1}) in negative potential window (-2~-0.6 V) and the discharge duration (158.9 F g^{-1}) in the positive part (-0.6~0.8 V) is comparable to that of GNS/*a*MWCNT@PDAA. Besides, the CV curves are in good accordance with the results for charge/discharge curves (Fig. S6b†). The above phenomena further confirm the viewpoint that PANI materials are principally used as the positive electrodes for organic supercapacitors due to the narrow potential window.[60,61] Surprisingly, due to unique p- and n-doping capability, the GNS/*a*MWCNT@PDAA can be commendably designed as both positive and negative electrodes for promising organic supercapacitors, which can result in excellent electrochemical performance. And the detailed charge/discharge schematic illustration was shown in Fig. 4c.

In order to take advantage of the broadest potential window and to avoid excessive charge/discharge, it is crucial to balance the charges ($q_+ = q_-$) stored at the positive and negative electrodes for GNS/*a*MWCNT@PDAA due to different redox reactions. The stored charges are related with the specific capacitance (*Cs*), the potential window (d*V*), and the mass (*m*) of the electrode according to $q = Cs \times dV \times m$. On the basis of the potential windows and specific capacitance values for negative and positive electrodes, the optimal mass ratio should be $m_+/m_- = 2$ in the present supercapacitor cell.

To estimate the optimal operating voltage of supercapacitor cell, a series of CV and charge/discharge measurements were carried out. Fig. 5a presents the CV curves with various potential windows for GNS/*a*MWCNT@PDAA supercapacitor. It is found that the as-fabricated supercapacitor shows a good capacitive behavior with quasi-rectangular CV curves even at the voltage up to 2.8 V. Nevertheless, the CV curve operated beyond 2.8 V

deviates seriously from rectangle shape, which is ascribed to severe polarization due to the degradation of PDAA. It is worth mentioning that the broad redox peaks are still robust enough at a superhigh scan rate of 2000 mV s⁻¹, indicating fast charge/discharge characteristics for high-power supercapacitor (Fig. 5b). Furthermore, the charge/discharge curves can remain a good symmetry at cell voltage as high as 2.8 V (Fig. 5c). This result closely corresponds to the coulombic efficiency, which all remains more than 89 % in the cell voltages of 2.2~2.8 V (Fig. 5d). Moreover, the specific capacitance gradually increases from 73.3 to 77.6 F g⁻¹ with the increase of cell voltages from 2.2 to 2.8 V, which means at least 171 % increase for stored energy and delivered power. Thus for comprehensive consideration, an operating voltage of 2.8 V is chosen for further investigation of the overall electrochemical performance for the supercapacitor in our subsequent research.
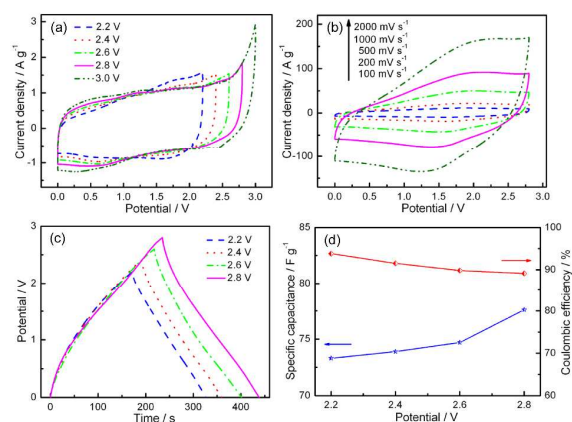

Fig. 5 Electrochemical performance of GNS/*a*MWCNT@PDAA supercapacitors in 1 M Et₄NBF₄-AN electrolyte. (a) CV curves at various potential windows at a scan rate of 10 mV s⁻¹. (b) CV curves at different scan rates. (c) Galvanostatic charge/discharge curves at various potential windows at a current density of 1 A g⁻¹. (d) Specific capacitances and coulombic efficiencies as a function of various potential windows.

To evaluate the electrochemical performance of GNS/*a*MWCNT@PDAA supercapacitor, pure PDAA was employed for comparison under the optimal voltage of 2.8 V. As seen from CV curves (Fig. 6a), the GNS/*a*MWCNT@PDAA clearly displays a combination of weak pseudocapacitive and predominant electrical double-layer types of capacitance rather than noticeable pseudocapacitive feature of pure PDAA. The charge curve of GNS/*a*MWCNT@PDAA supercapacitor is almost symmetrical to the corresponding discharge curve with a good linear voltage-time profile (Fig. 6b). Moreover even at high current densities, the charge/discharge curves for GNS/*a*MWCNT@PDAA still show little IR drop, but much for the PDAA (Fig. S7†). These phenomena demonstrate rapid *I-V* response and ideal capacitive characteristics of the nanocomposite. Furthermore, the calculations based on total mass of both electrodes indicate that the GNS/*a*MWCNT@PDAA supercapacitor exhibits higher specific capacitance (80.8 F g⁻¹ at 0.5 A g⁻¹), which is superior to that of other organic supercapacitor cells (if the three-electrode system, the specific capacitance should be transformed into that of two-electrode cells).[62-65] As seen from Fig. 6c, the nanocomposite retains 65 %

capacitance (52.5 F g⁻¹) at high current density of 100 A g⁻¹, indicating outstanding rate capability. In contrast, pure PDAA loses 75.3 % (51.5 to 12.7 F g⁻¹) of its initial capacitance as the current density is increased from 0.5 to 20 A g⁻¹. It is ascribed to considerable enhancement of the conductivity (1.36 S cm⁻¹) for GNS/*a*MWCNT@PDAA, much higher than that for PDAA (1.15×10⁻³ S cm⁻¹).
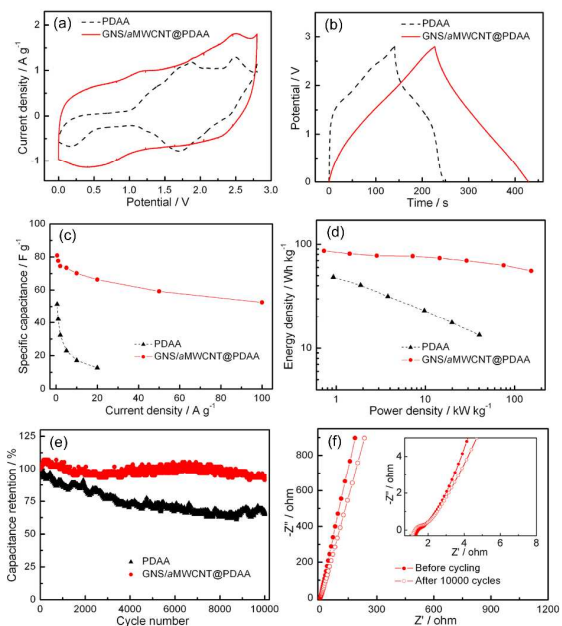

Fig. 6 Electrochemical performance of supercapacitors based on PDAA and GNS/*a*MWCNT@PDAA in 1 M Et₄NBF₄-AN electrolyte. (a) CV curves at a scan rate of 10 mV s⁻¹. (b) Galvanostatic charge/discharge curves at a current density of 1 A g⁻¹. (c) Specific capacitances as a function of various current densities. (d) Ragone plots. (e) Cycling stability at a current density of 1 A g⁻¹. (f) Nyquist plots of GNS/*a*MWCNT@PDAA before cycling and after 10000 cycles.

More importantly, the GNS/*a*MWCNT@PDAA supercapacitor also exhibits superhigh energy and power densities. As shown in Fig. 6d, the maximum energy density of 86.4 Wh kg⁻¹ is achieved at a power density of 0.73 kW kg⁻¹, and still retains 55.5 Wh kg⁻¹ even at superhigh power density of 153.9 kW kg⁻¹. For comparison, the PDAA supercapacitor delivers a much lower energy density of 13.3 Wh kg⁻¹ at 40.3 kW kg⁻¹. Moreover, the high energy density for GNS/*a*MWCNT@PDAA supercapacitor is much higher than recently reported supercapacitors in organic electrolytes,[22,61-69] which are mainly listed in Tab. 1, such as poly(DAAQ)//poly(DAAQ) (25 Wh kg⁻¹, 30.5 kW kg⁻¹),[22] ACNT@PANI//ACNT@PANI (18.1 Wh kg⁻¹, 0.11 kW kg⁻¹),[62] H₂Ti₆O₁₃//CMK-3 (< 2 Wh kg⁻¹, 11 kW kg⁻¹),[66] HMC-800//HMC-800 (29 Wh kg⁻¹, 2.24 kW kg⁻¹),[63] a-MEGO//a-MEGO (39 Wh kg⁻¹, 145 kW kg⁻¹)[64] and 3D HPG//3D HPG (38 Wh kg⁻¹, ~8 kW kg⁻¹).[65] The remarkable enhancements in both energy and power densities of the GNS/*a*MWCNT@PDAA supercapacitor can be attributed to excellent conductivity of GNS/*a*MWCNT carrier, unique p- and n-doping characteristic of PDAA, hierarchical porous structure of the nanocomposite and wide cell voltage of 2.8 V in organic electrolyte.

Tab. 1 Comparison of the electrochemical performances of the supercapacitors based on GNS/*a*MWCNT@PDAA and other recently reported supercapacitors in organic system.

Electrode materials	Electrolytes	Energy density	Cycling stability	Ref.
GNS/*a*MWCNT@PDAA// GNS/*a*MWCNT@PDAA	1 M Et$_4$NBF$_4$ in AN (2.8 V)	86.4 Wh kg^{-1} (0.73 kW kg^{-1}) 55.5 Wh kg^{-1} (153.9 kW kg^{-1})	93 % (10000 cycles)	This work
CCG//CCG	EMIMBF$_4$ (3.5 V)	/	over 95 % (300 hr)	[3]
poly(DAAQ)//poly(DAAQ)	1 M TEAClO$_4$ in PC (2.3 V)	46 Wh kg^{-1} (10.2 kW kg^{-1}) 25 Wh kg^{-1} (30.5 kW kg^{-1})	/	[22]
Li(Mn$_{1/3}$Ni$_{1/3}$Fe$_{1/3}$)O$_2$- PANI//AC	1 M LiPF$_6$ in EC/DMC (3 V)	49 Wh kg^{-1} (*ca.* 1 kW kg^{-1})	/	[61]
ACNT@PANI//ACNT@PANI	1 M LiPF$_6$ in EC/DEC (2.5 V)	18.1 Wh kg^{-1} (0.11 kW kg^{-1})	95 % (2000 cycles)	[62]
HMC-800//HMC-800	1 M LiPF$_6$ in EC/DEC (3 V)	45.3 Wh kg^{-1} (*ca.* 0.08 kW kg^{-1}) 29 Wh kg^{-1} (2.24 kW kg^{-1})	98 % (20000 cycles)	[63]
a-MEGO//a-MEGO	1M TEABF$_4$ in AN (2.7 V)	39 Wh kg^{-1} (145 kW kg^{-1})	/	[64]
3D HPG//3D HPG	1 M TEMABF$_4$ in PC (2.5 V)	38 Wh kg^{-1} (*ca.* 8 kW kg^{-1})	*ca.* 100 % (10000 cycles)	[65]
H$_2$Ti$_6$O$_{13}$//CMK-3	1 M LiPF$_6$ in EC/EDC (3.5 V)	< 2 Wh kg^{-1} (11 kW kg^{-1})	80 % (1000 cycles)	[66]
curved graphene// curved graphene	EMIMBF$_4$ (4 V)	53.1 Wh kg^{-1} (9.8 kW kg^{-1})	/	[67]
MoO$_3$/MWCNT//MoO$_3$/MWCNT	1 M LiClO$_4$ in PC (1.8 V)	38.7 Wh kg^{-1} (0.33 kW kg^{-1}) 36.6 Wh kg^{-1} (1.87 kW kg^{-1})	80 % (1000 cycles)	[68]
PSDAC-800-3//PSDAC-800-3	BMPY TFSI and EMIM TFSI (3 V)	51 Wh kg^{-1} (0.38 kW kg^{-1}) 26-31 Wh kg^{-1} (6.8~7 kW kg^{-1})	91 % (5000 cycles)	[69]

The cycling stability is further investigated by consecutive galvanostatic charge/discharge cycling within 0~2.8 V at a current density of 1 A g^{-1}. As shown in Fig. 6e, the PDAA supercapacitor retains 66 % of its initial capacitance after 10000 cycles. Surprisingly, only 7 % capacitance deterioration is achieved for the GNS/*a*MWCNT@PDAA, demonstrating superior long-term electrochemical stability. Such cycling performance is much superior to that of pseudocapacitive supercapacitors in organic systems (Tab. 1).[62,66,68] The outstanding cycling stability can be explained as follows: 1) Less mechanical degradation by isotropic lattice expansion and shrinkage of peculiar π-stacked PDAA "supramolecule". 2) Nano-size and porous structure of the PDAA facilitate the transport of electrolyte ions and provide a large accessible surface area, which greatly relieve the volumetric changes during charge/discharge process. 3) Strong π-π interaction between the PDAA and GNS/*a*MWCNT with exceptional mechanical performance supplies good elasticity to accommodate the strain of volumetric changes. 4) Stable potential window and suitable mass ratio of both electrodes can avoid excessive charge/discharge and effectively prevent the degradation of PDAA.

In order to verify the cycling stability, electrochemical impedance was measured before and after 10000 cycles. As seen from the inset of Fig. 6f, it is apparent that the GNS/*a*MWCNT@PDAA exhibits an almost unchanged circular arc corresponding to charge transfer resistance (R$_{CT}$) and displays only little inclined tendency for the straight line after 10000 cycles. However, the straight line for PDAA displays an obvious incline towards X axis after cycling (Fig. S8†). In addition, the charge/discharge curve tested after cycling shows no obvious

increase for the IR drop of GNS/*a*MWCNT@PDAA (Fig. S9†). Therefore, the above analysis provides powerful supports for superior cycling stability of the GNS/*a*MWCNT@PDAA supercapacitor.

4. Conclusions

In summary, a novel GNS/*a*MWCNT@PDAA nanocomposite with hierarchical nanoporous structure was successfully synthesized. The as-fabricated GNS/*a*MWCNT@PDAA supercapacitor in 1 M Et$_4$NBF$_4$-AN electrolyte can be reversibly cycled in potential window of 2.8 V and exhibits high energy density of 86.4 Wh kg^{-1} at a power density of 0.73 kW kg^{-1}, which still retains 55.5 Wh kg^{-1} even at superhigh power density of 153.9 kW kg^{-1}. Furthermore, excellent cycling stability with 93 % capacitance retention is also achieved after 10000 cycles. The above remarkable performance has come up to the state-of-the-art level, which is superior to that of most recently reported organic supercapacitors and also comparable to that of Nickel-metal hydride (Ni-MH) batteries. In addition, such high power density far surpasses the power target in hybrid vehicles, thus supporting the applicability as power supply components. These encouraging findings open up the possibility of π-conjugated polymers for advanced organic supercapacitors, which commendably meet versatile demands for available power and energy characteristics.

Acknowledgements

Notes and references

a Shanghai Key Laboratory of Advanced Polymeric Materials, Key Laboratory for Ultrafine Materials of Ministry of Education, School of Materials Science and Engineering, East China University of Science and Technology, Shanghai 200237, P.R.China. E-mail: gengchaow@ecust.edu.cn

1   P. Simon and Y. Gogotsi, *Nat. Mater.*, 2008, **7**, 845-854.
2   W. F. Wei, X. W. Cui, W. X. Chen and D. G. Ivey, *Chem. Soc. Rev.*, 2011, **40**, 1697-1721.
3   X. W. Yang, C. Cheng, Y. F. Wang, L. Qiu and D. Li, *Science*, 2013, **341**, 534-537.
4   H. Jiang, P. S. Lee and C. Z. Li, *Energy Environ. Sci.*, 2013, **6**, 41-53.
5   L. Nyholm, G. Nyström, A. Mihranyan and M. Strømme, *Adv. Mater.*, 2011, **23**, 3751-3769.
6   F. Zhang, C. Z. Yuan, J. J. Zhu, J. Wang, X. G. Zhang and X. W. Lou, *Adv. Funct. Mater.*, 2013, **23**, 3909-3915.
7   J. Xu, Q. F. Wang, X. W. Wang, Q. Y. Xiang, B. Liang, D. Chen and G. Z. Shen, *ACS Nano*, 2013, **7**, 5453-5462.
8   L. L. Zhang and X. S. Zhao, *Chem. Soc. Rev.*, 2009, **38**, 2520-2531.
9   J. S. Lee, C. Lee, J. Jun, D. H. Shin and J. Jang, *J. Mater. Chem. A*, 2014, **2**, 11922-11929.
10 X. Lu, M. Yu, G. Wang, T. Zhai, S. Xie, Y. Ling, Y. Tong and Y. Li, *Adv. Mater.*, 2012, **25**, 267-272.
11 P. C. Chen, G. Shen, Y. Shi, H. Chen and C. Zhou, *ACS Nano*, 2010, **4**, 4403-4411.
12 C. Z. Meng, C. H. Liu, L. Z. Chen, C. H. Hu and S. S. Fan, *Nano Lett.*, 2010, **10**, 4025-4031.
13 Q. Wu, Y. X. Xu, Z. Y. Yao, A. R. Liu and G. Q. Shi, *ACS Nano*, 2010, **4**, 1963-1970.
14 B. G. Choi, J. Hong, W. H. Hong, P. T. Hammond and H. Park, *ACS Nano*, 2011, **5**, 7205-7213.
15 A. Razaq, L. Nyholm, M. Sjödin, M. Strømme and A. Mihranyan, *Adv. Energy Mater.*, 2012, **2**, 445-454.
16 J. T. Zhang, J. W. Jiang, H. L. Li and X. S. Zhao, *Energy Environ. Sci.*, 2011, **4**, 4009-4015.
17 J. L. Shen, C. Y. Yang, X. W. Li and G. C. Wang, *ACS Appl. Mater. Interfaces*, 2013, **5**, 8467-8476.
18 Y. S. Zhao, J. S. Wu and J. X. Huang, *J. Am. Chem. Soc.*, 2009, **131**, 3158-3159.
19 V. Noël and H. N. Randriamahazaka, *Electrochem. Commun.*, 2012, **19**, 32-35.
20 H. Y. Liu, G. Q. Zhang, Y. F. Zhou, M. M. Gao and F. L. Yang, *J. Mater. Chem. A*, 2013, **1**, 13902-13913.
21 S. Suematsu and K. Naoi, *J. Power Sources*, 2001, **97-98**, 816-818.
22 K. Naoi, S. Suematsu and A. Manago, *J. Electrochem. Soc.*, 2000, **147**, 420-426.
23 X. G. Li, H. Li and M. R. Huang, *Chem. Eur. J.*, 2007, **13**, 8884-8896.
24 K. Naoi, S. Suematsu, M. Hanada and H. Takenouchi, *J. Electrochem. Soc.*, 2002, **149**, A472-A477.
25 S. A. Hashmi, S. Suematsu and K. Naoi, *J. Power Sources*, 2004, **137**, 145-151.
26 M. Q. Sun, Q. Q. Tang, T. Zhang and G. C. Wang, *RSC Adv.*, 2014, **4**, 7774-7779.
27 M. M. Gao, F. L. Yang, X. H. Wang, G. Q. Zhang and L. F. Liu, *J. Phys. Chem. C*, 2007, **111**, 17268-17274.
28 C. R. Pérez, S. H. Yeon, J. Ségalini, V. Presser, P. L. Taberna, P. Simon and Y. Gogotsi, *Adv. Funct. Mater.*, 2013, **23**, 1081-1089.
29 N. Nuraje, K. Su, N. Yang and H. Matsui, *ACS Nano*, 2008, **2**, 502-506.
30 B. K. Kuila, B. Nandan, M. Bёhme, A. Janke and M. Stamm, *Chem. Commun.*, 2009, **38**, 5749-5751.
31 X. M. Zhu, L. Q. Wang, J. P. Lin and L. S. Zhang, *ACS Nano*, 2010, **4**, 4979-4988.
32 B. Ma, X. Zhou, H. Bao, X. W. Li and G. C. Wang, *J. Power Sources*, 2012, **215**, 36-42.
33 J. L. Liu, L. L. Zhang, H. B. Wu, J. Y. Lin, Z. X. Shen and X. W. Lou, *Energy Environ. Sci.*, 2014, **7**, 3709-3719.
34 Y. Z. Liao, C. Zhang, Y. Zhang, V. Strong, J. S. Tang, X. G. Li, K. Kalantar-zadeh, E. M. V. Hoek, K. L. Wang and R. B. Kaner, *Nano Lett.*, 2011, **11**, 954-959.
35 Y. G. Wang, H. Q. Li and Y. Y. Xia, *Adv. Mater.*, 2006, **18**, 2619-2623.
36 P. A. Mini, A. Balakrishnan, S. V. Nair and K. R. V. Subramanian, *Chem. Commun.*, 2011, **47**, 5753-5755.
37 N. A. Kumar, H. J. Choi, Y. R. Shin, D. W. Chang, L. M. Dai and J. B. Baek, *ACS Nano*, 2012, **6**, 1715-1723.
38 H. L. Wang, Q. L. Hao, X. J. Yang, L. D. Lu and X. Wang, *Nanoscale*, 2010, **2**, 2164-2170.
39 Y. N. Meng, K. Wang, Y. J. Zhang and Z. X. Wei, *Adv. Mater.*, 2013, **25**, 6985-6990.
40 W. Chen, R. B. Rakhi and H. N. Alshareef, *Nanoscale*, 2013, **5**, 4134-4138.
41 X. Li and I. Zhitomirsky, *J. Power Sources*, 2013, **221**, 49-56.
42 J. F. Che, P. Chen and M. B. Chan-Park, *J. Mater. Chem. A*, 2013, **1**, 4057-4066.
43 T. M. Wu, Y. W. Lin and C. S. Liao, *Carbon*, 2005, **43**, 734-740.
44 C. Z. Meng, C. H. Liu and S. S. Fan, *Electrochem. Commun.*, 2009, **11**,186-189.
45 Z. Q. Niu, P. S. Luan, Q. Shao, H. B. Dong, J. Z. Li, J. Chen, D. Zhao, L. Cai, W. Y. Zhou, X. D. Chen and S. S. Xie, *Energy Environ. Sci.*, 2012, **5**, 8726-8733.
46 L. Z. Fan, Y. S. Hu, J. Maier, P. Adelhelm, B. Smarsly and M. Antonietti, *Adv. Funct. Mater.*, 2007, **17**, 3083-3087.
47 L. X. Li, H. H. Song, Q. C. Zhang, J. Y. Yao and X. H. Chen, *J. Power Sources*, 2009, **187**, 268-274.
48 X. J. Lu, H. Dou, S. D. Yang, L. Hao, L. J. Zhang, L. F. Shen, F. Zhang and X. G. Zhang, *Electrochim. Acta*, 2011, **56**, 9224-9232.
49 J. Yan, T. Wei, Z. J. Fan, W. Z. Qian, M. L. Zhang, X. D. Shen and F. Wei, *J. Power Sources*, 2010, **195**, 3041-3045.
50 S. P. Zhou, H. M. Zhang, X. H. Wang, J. Li and F. S. Wang, *RSC Adv.*, 2013, **3**, 1797-1807.
51 M. K. Liu, Y. E. Miao, C. Zhang, W. W. Tjiu, Z. B. Yang, H. S. Peng and T. X. Liu, *Nanoscale*, 2013, **5**, 7312-7320.
52 M. A. Worsley, P. J. Pauzauskie, T. Y. Olson, J. Biener, J. H. Satcher and T. F. Baumann, *J. Am. Chem. Soc.*, 2010, **132**, 14067-14069.
53 X. L. Wu, T. Wen, H. L. Guo, S. B. Yang, X. K. Wang and A. W. Xu, *ACS Nano*, 2013, **7**, 3589-3597.
54 H. C. Chien, W. Y. Cheng, Y. H. Wang and S. Y. Lu, *Adv. Funct. Mater.*, 2012, **22**, 5038-5043.
55 W. S. Hummers and R. E. Offeman, *J. Am. Chem. Soc.*, 1958, **80**, 1339-1339.
56 I. D. Rosca, F. Watari, M. Uo and T. Akaska, *Carbon*, 2005, **43**, 3124-3131.
57 M. Q. Sun, G. C. Wang, X. W. Li and C. Z. Li, *J. Power Sources*, 2014, **245**, 436-444.
58 H. Zengin, W. S. Zhou, J. Y. Jin, R. Czerw, D. W. Smith, L. Echegoyen, D. L. Carroll, S. H. Foulger and J. Ballato, *Adv. Mater.*, 2002, **14**, 1480-1483.
59 Z. Z. Zhu, G. C. Wang, M. Q. Sun, X. W. Li and C. Z. Li, *Electrochim. Acta*, 2011, **56**, 1366-1372.
60 S. P. Zhou, H. M. Zhang, Q. Zhao, X. H. Wang, J. Li and F. S. Wang, *Carbon*, 2013, **52**, 440-450.
61 K. Karthikeyan, S. Amaresh, V. Aravindan, H. Kim, K. S. Kang and Y. S. Lee, *J. Mater. Chem. A*, 2013, **1**, 707-714.
62 F. Huang, F. L. Lou and D. Chen, *ChemSusChem*, 2012, **5**, 888-895.
63 W. J. Qian, F. X. Sun, Y. H. Xu, L. H. Qiu, C. H. Liu, S. D. Wang and F. Yan, *Energy Environ. Sci.*, 2014, **7**, 379-386.
64 Y. W. Zhu, S. Murali, M. D. Stoller, K. J. Ganesh, W. W. Cai, P. J. Ferreira, A. Pirkle, R. M. Wallace, K. A. Cychosz, M. Thommes, D. Su, E. A. Stach and R. S. Ruoff, *Science*, 2011, **332**, 1537-1541.
65 Y. Y. Li, Z. S. Li and P. K. Shen, *Adv. Mater.*, 2013, **25**, 2474-2480.
66 Y. G. Wang, Z. S. Hong, M. D. Wei and Y. Y. Xia, *Adv. Funct. Mater.*, 2012, **22**, 5185-5193.
67 C. G. Liu, Z. N. Yu, D. Neff, A. Zhamu and B. Z. Jang, *Nano Lett.*, 2010, **10**, 4863-4868.
68 Q. Mahmood, H. J. Yun, W. S. Kim and H. S. Park, *J. Power Sources*, 2013, **235**, 187-192.
69 H. L. Wang, Z. Li, J. K. Tak, C. M. B. Holt, X. H. Tan, Z. W. Xu, B. S. Amirkhiz, D. Harfield, A. Anyia, T. Stephenson and D. Mitlin, *Carbon*, 2013, **57**, 317-328.

Table of contents

Colour graphic

- ● **DAA/CSA complex**   ■ **PDAA nanoparticles**   ○ **mesopores**
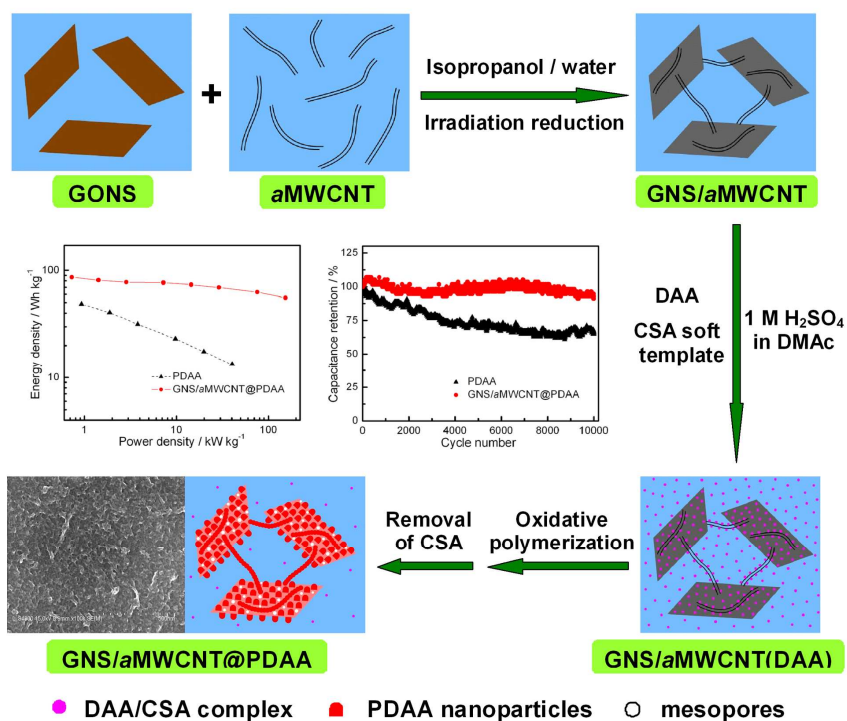
Text

An intriguing organic supercapacitor based on hierarchical porous GNS/*a*MWCNT@poly(1,5-diaminoanthraquinone) is fabricated with superhigh energy density and excellent cycling stability.